Impact of surface defects on $LaNiO_3$ perovskite electrocatalysts for oxygen evolution reaction

Hamidreza Arandiyan,[a, b*] Sajjad S. Mofarah,[c] Yuan Wang,[a,b,d*] Claudio Cazorla,[e] Deshetti Jampaiah,[b] Magnus Garbrecht,[f] Karen Wilson,[b] Adam F. Lee,[b] Chuan Zhao,[d] Thomas Maschmeyer[a*]

Dr. Hamidreza Arandiyan, Prof. Thomas Maschmeyer
[a] *Laboratory of Advanced Catalysis for Sustainability, School of Chemistry, University of Sydney, Sydney, NSW 2006, Australia*
E-mail: thomas.maschmeyer@sydney.edu.au

Dr. Hamidreza Arandiyan, Dr. Yuan Wang, Dr. Deshetti Jampaiah, Prof. Karen Wilson, Prof. Adam F. Lee
[b] *Centre for Advanced Materials & Industrial Chemistry (CAMIC), School of Science, RMIT University, Melbourne, VIC, 3000, Australia*
E-mail: hamid.arandiyan@rmit.edu.au

Dr. Sajjad S. Mofarah
[c] *School of Materials Science and Engineering, UNSW Sydney, Sydney, NSW 2052, Australia*

Dr. Yuan Wang, Prof. Chuan Zhao
[d] *School of Chemistry, UNSW Sydney, Sydney, NSW 2052, Australia*
Email: yuan.wang@rmit.edu.au

Dr. Claudio Cazorla
[e] *Departament de Física, Universitat Politècnica de Catalunya, Campus Nord B4-B5, E-08034 Barcelona, Spain*

Dr. Magnus Garbrecht
[f] *Australian Centre for Microscopy and Microanalysis, The University of Sydney, Sydney, NSW, 2006 Australia*

Hamidreza Arandiyan and Sajjad S. Mofarah contributed equally to this work.

Keywords: Surface defects; Electrocatalysts; Perovskite; Oxygen evolution reaction

Highlights

- High concentration of surface defects generated through thermal reduction.
- Impact of defects on oxygen evolution reaction (OER) investigated.
- Surface oxygen vacancies promote OER over macroporous $LaNiO_3$.
- Defective $LaNiO_3$ is stable and more active than a benchmark IrO_2 electrocatalyst.

Abstract

Perovskite oxides are regarded as promising electrocatalysts for water splitting due to their cost-effectiveness, high efficiency and durability in the oxygen evolution reaction (OER). Despite these advantages, a fundamental understanding of how critical structural parameters of perovskite electrocatalysts influences their activity and stability is lacking. Here, we investigate the impact of structural defects on OER performance for representative $LaNiO_3$ perovskite electrocatalysts. Hydrogen reduction of 700 °C calcined $LaNiO_3$ induces a high density of surface oxygen vacancies, and confers significantly enhanced OER activity and stability compared to unreduced $LaNiO_3$; the former exhibit a low onset overpotential of 380 mV at 10 $mA.cm^{-2}$ and a small Tafel slope of 70.8 $mV.dec^{-1}$. Oxygen vacancy formation is accompanied by mixed Ni^{2+}/Ni^{3+} valence states, which quantum-chemical DFT calculations reveal modify the perovskite electronic structure. Surface oxygen vacancy formation is relatively facile, and favoured over lattice vacancy formation, and increases the electronic conductivity of reduced $LaNiO_3$, in accordance with the enhanced OER activity observed.

1. Introduction

Efficient oxygen evolution reaction (OER) is an important goal for renewable energy technologies including metal-O_2 batteries ($M_xO_2 \rightarrow M_x + O_2$), [1, 2] electrolytic water splitting ($H_2O \rightarrow H_2 + ½O_2$), [3] and reversible fuel cells. [4] Unfortunately, the sluggish intrinsic kinetics of OER hampers the development of associated energy devices. [5-7] IrO_2 and RuO_2 are current benchmark electrocatalysts for OER in alkaline and acidic medium, however their scarcity and high cost have limited practical applications, [6] and hence the development of noble metal-free OER electrocatalysts is urgently sought. Perovskite oxides have great potential as electrocatalysts for OER in alkaline electrolytes due to their versatile physicochemical properties and elemental abundance. Perovskite oxides of formula ABO_3 comprise alkaline earth and rare earth metals in the A site and 3d transition metals in the B site. [8] To date, research has focused on perovskites such as $LaCoO_3$, [9] $(La_{0.6}Sr_{0.4})FeO_3$, [10] $(Ba_{0.5}Sr_{0.5})(Co_{0.8}Fe_{0.2})O_3$, [11] and $(La_{0.2}Sr_{0.8})(Co_{0.8}Fe_{0.2})O_3$ which show promising electrocatalytic activity for OER. $LaNiO_3$ (LNO) in particular exhibits metal-like electrical conductivity and an OER activity close to the maximum predicted from volcano rate plots. [11] Despite the low surface area (< 4

m^2/g) of non-porous LNO, its catalytic OER activity can reach 370 $\mu A.cm^2$, [12] close to the benchmark value of 500 $\mu A/cm^2$ reported for high area (>70 m^2/g) IrO_2. [13] However, the high intrinsic OER activity of LNO is offset by the low specific surface area obtained by conventional synthetic routes; [14] facile methods to synthesise high area perovskite oxides are hence required.

Previous research has identified a stable low-spin (LS) e_g^1 configuration of LNO as critical to its robust stability under a range of potentials. [15] However, recent evidence suggests that substitution of alien elements at A and B sites to break this stable configuration can further improve the electrocatalytic activities of perovskite oxides. [16-18] Petrie et al [19] demonstrated the impact of strain in LNO thin films, achieving significant enhancements in the OER and oxygen reduction reaction. Strain-induced splitting of e_g orbitals can modulate orbital asymmetry at the perovskite surface and contribute to improved activity. The introduction of oxygen vacancies into perovskite oxides can also tune their electronic structure and ion/electronic conductivity, thereby enhancing OER performance. [20, 21] Wang et al [22] developed a surface defective 3D inverse opal $LaCoO_{3-x}$ perovskite electrocatalyst wherein abundant defects modified the density of electronic states at the surface and d-band center of Co states, increasing the corresponding turnover frequency (TOF) for OER 10-fold versus a non-defective counterpart. Zhao et al [23] demonstrated the fabrication of binder-free $LaCoO_3$ nanosheets vertically grown on a conductive nickel foam electrode with a high electrocatalytic surface area (following hydrothermal treatment and annealing). The resulting electrocatalysts achieved a current density of 10 $mA.cm^{-2}$ at 342 mV overpotential, attributed to a high density of surface oxygen vacancies and surface hydrophilicity (promoting gas bubbles dissipation).

Defects in perovskite materials can decrease the oxygen migration energy and increase the density of surface oxygen vacancies, generating unique active sites which enhance OER catalytic activity. Cation doping can tune perovskite oxides to control oxygen vacancies. Sun et al incorporated Ce into $LaNiO_3$ to promote surface self-reconstruction,[24] observing that: (i) oxygen vacancies were generated by Ce doping in the resulting $La_{1-x}Ce_xNiO_3$ perovskite; and (ii) surface self-reconstruction was responsible for an increased OER activity. A 10% Ce doped $LaNiO_3$ exhibited ~32 times greater mass activity with 270 mV overpotential (at

10 mA cm^{-2}) and a Tafel slope of 45 mV dec^{-1} than pristine $LaNiO_3$ oxides. Choi et al also studied the effect of strain and cation deficiency in $LaNiO_3$ perovskite for OER.[25] Manipulating the NiO_6 octahedral structure in $LaNiO_3$ perovskite by introducing a 5% La deficiency induced a larger Ni–O–Ni bond angle and narrower charge transfer gap, whereas A-site deficient $LaNiO_3$ exhibited lower OER activity. Mismatch segregation of the dopant and lattice ions resulted from strain between the substrate and perovskite thin film. Synergy arising from an A-site deficiency and compressive strain in the $La_{0.95}NiO_3$ catalyst greatly enhanced OER activity compared to pristine $LaNiO_3$. Rational design of high-performance electrocatalysts through defect engineering necessitates a deeper understanding of the relationship between defects and electrocatalytic activity. Thermal reduction in a reducing atmosphere (typically H_2, NH_3 or CO), is a common strategy to generate structural defects in perovskites. A layered double perovskite $PrBaMn_2O_{6-\delta}$ fabricated by hydrogen treatment at 800 °C, evidenced a high concentration of oxygen vacancies and associated high gravimetric and volumetric capacitance. [26] Previous structural and electrochemical analyses indicate that oxygen vacancies promote OER performance of perovskite oxides,[27] in part due to changes in their electronic structure.[28] However, such studies have not considered the relative importance of surface versus lattice oxygen vacancies on perovskite electrocatalysts.[29]

Herein, LNO electrocatalysts were fabricated by a sol-gel method, incorporating cetyl ammonium bromide (CTAB) cationic and citric acid as respective structure directing and chelating agents (to improve porosity and thermal processing [30]) and subsequent calcination (**Scheme 1**). Resulting materials were designated LNO-700 and LNO-900, and the impact of hydrogen reduction on the LNO-700 material (to generate red-LNO-700) was also explored. High temperature calcination yields a low porosity material with pore activity for the electrochemical oxygen evolution reaction. Reduction of LNO calcined at lower temperature confers a superior OER performance attributed to the formation of surface defects, notably oxygen vacancies, and an enhanced electrochemically active surface area, which improved electrical conductivity and interfacial charge transfer offering better activity and long-term stability at lower overpotential. DFT calculations support the facile formation of oxygen defects in LNO surfaces and indicate that reduced LNO surfaces

should exhibit increased electrical conductivity. Our facile synthesis and activation protocol offers a potential route to high efficiency perovskite electrocatalysts for renewable energy applications.

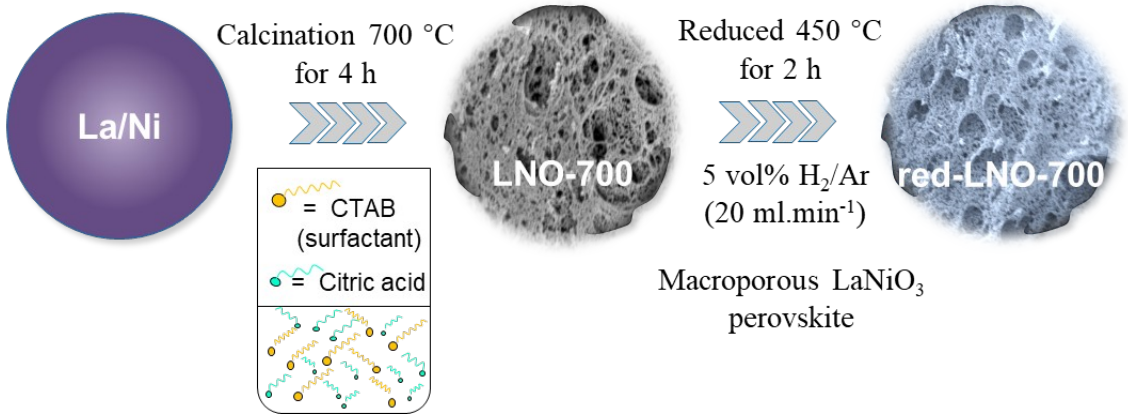

Scheme 1. Synthesis of red-LNO-700.

2. Results and Discussion

Scanning electron microscopy (SEM) imaging (**Fig. S1a-c**) evidences open macroporous structures for all LNO materials, likely associated with CTAB addition during the sol-gel step in accordance with literature reports. [31] The red-LNO-700 exhibited a foam-like morphology with a smoother external surface. Porosimetry revealed type V isotherms with H3 hysteresis loops (p/p_0 = 0.8-1.0) for LNO-700 and red-LNO-700 materials (**Fig. 1a**) as anticipated for macroporous solids. [32] BET surface areas and pore volumes of all materials were very low (7 $m^2.g^{-1}$ and <0.05 $cm^3.g^{-1}$, **Table S1**), with 900 °C calcination resulting in almost a complete loss of porosity. Powder X-ray diffraction (XRD) evidences reflections characteristic of rhombohedral $LaNiO_3$ (JCPDS PDF 01-088-0633) for all materials (**Fig. 1b**), however red-LNO-700 also exhibits a reflection indicative of NiO consistent with partial reduction of the perovskite following hydrogen treatment. Such partial reduction of perovskite oxides can also induce structural defects.[17] Average $LaNiO_3$ crystallite sizes estimated using the Debye–Scherrer equation (**Table S1**) reveal similar dimensions for LNO-700 and red-LNO-700 of 10.3 nm and 12.1 nm respectively, whereas that for LNO-900 was 16.8 nm presumably due to aggregation of small particles at the higher calcination temperature.

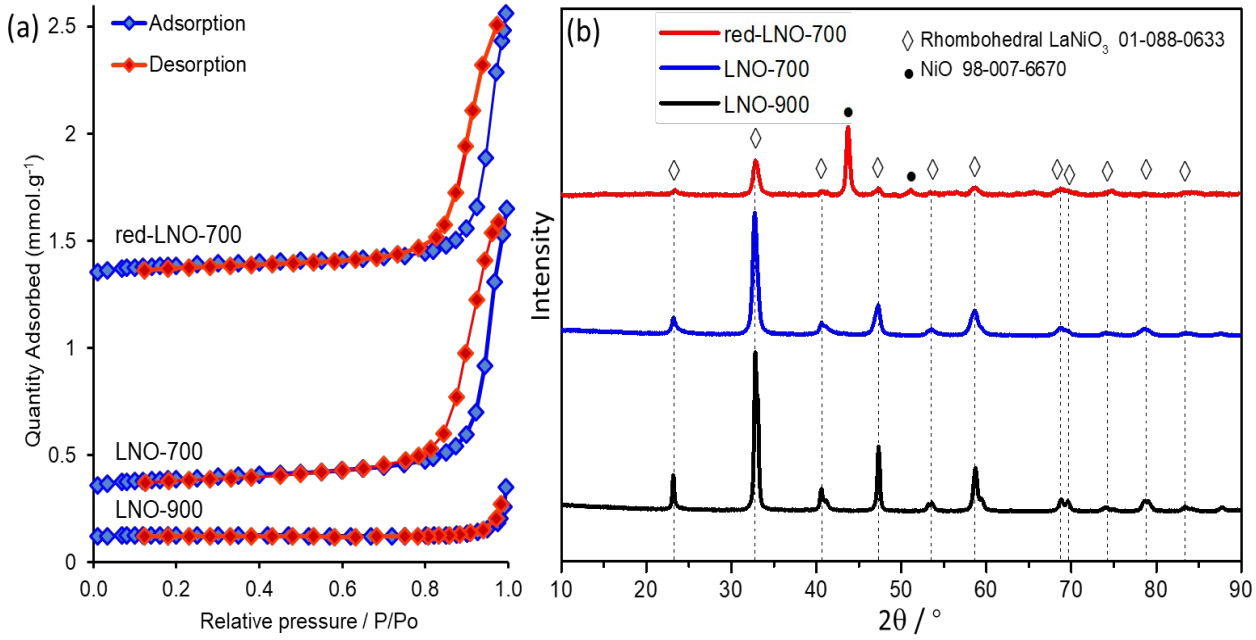

Fig. 1. (a) N_2 adsorption-desorption isotherms (offset by 0.1, 0.3 and 1.3 mmol.g^{-1} for clarity) and (b) XRD patterns of LNO materials (offset for clarity).

The presence of surface defects on red-LNO-700 was subsequently explored by high-angle annular dark-field scanning transmission electron microscopy (HAADF-STEM). Although red-LNO-700 exhibits lattice fringes with a 0.38 nm spacing, consistent with the [012] plane of rhombohedral $LaNiO_3$, many randomly distributed and irregular domains of different contrast are also apparent (**Fig. 2a**). Selected enlarged areas of **Fig. 2a** are illustrated in **Fig. 2b,d** (area I) and **Fig. 2c,e** (area II). Close observation reveals that these domains arise from half shifts of the unit cell in the [012] direction (stacking faults) and missing NiO_2 units, which result in zigzag arrays of lanthanum atoms characteristic of Ruddlesden-Popper (RP) phases (see highlighted red region in **Fig. 2d**), as described by Detemple et al. [33] The zigzag domain boundary is composed of many vertical and horizontal atomic steps in the [012] direction at the atomic level. These atomic steps in red-LNO-700 result in island-like features surrounded by the RP phase (**Fig. 2b,c**). Comparing against perfect $LaNiO_3$ domains in **Fig. 2e**, the relative displacement of A and B is 1/2a[012] (half unit) in the defective domains, with the rock salt (LaO_2) structure apparent on defect boundaries (**Fig. 2d**). Energy dispersive spectroscopy (EDS) maps and line profiles (**Fig. 2f-i** and **Fig. S3**) show a uniform distribution of La, Ni and O elements in red-LNO-700. The fast Fourier transfer (FFT) pattern (**Fig. 2j**) of

the domain in **Fig. 2e** reveals reflections characteristic of [012], [110], [202], [024], and [122] planes of $LaNiO_3$ perovskite, in accordance with XRD (**Fig. 1b**). No defects were observed for LNO-700 or LNO-900 materials (**Fig. S2a,b**)

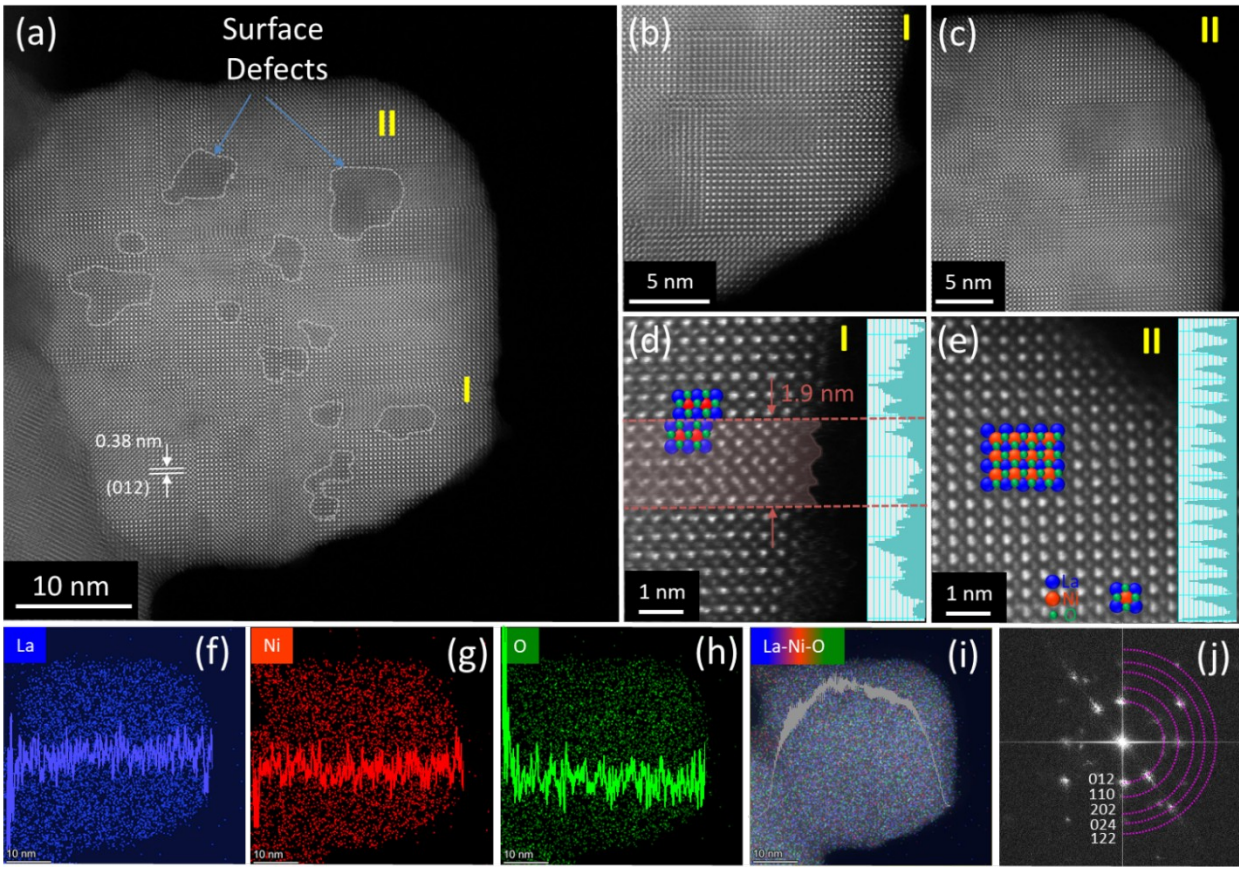

Fig. 2. (a) HAADF-STEM image of red-LNO-700, (b-e) enlarged images of zones I and II (insets are line profiles extracted from corresponding TEM images), (f-i) EDS elemental mapping and (j) corresponding fast Fourier transform (FFT) of HAADF-STEM image in (e).

Temperature-programmed oxygen desorption (O_2-TPD) of LNO materials was explored to provide additional insight into the nature of oxygen vacancies and energetics of their formation. LNO-700 and LNO-900 were thermally stable to 650 °C (**Fig. 3a)**, above which a small, well-defined oxygen desorption was observed for LNO-700 (T_{max} = 739 °C), with both materials exhibiting a large oxygen desorption at a common higher temperature (T_{max} ≈ 955 °C). The former desorption, typically designated α-O_2, originates from near-surface oxygen, whereas the latter, β-O_2, arises from the loss of lattice oxygen (O_{latt}). [34, 35] Hydrogen treatment (red-LNO-700) significantly increases both the magnitude of oxygen desorption and α-

versus β-O_2 desorption and lowers the respective desorption temperatures for each molecular species (T_{max} = 679 °C and 733 °C). Collectively, these observations demonstrate that LNO reduction increases the concentration and stability of surface oxygen vacancies, with concomitant destabilisation of lattice oxygen. O 1s XP spectra (**Fig. 3b**) confirm the impact of reduction on surface oxygen species. All materials exhibit four distinct oxygen chemical environments centred at 528.2, 530.4, 531.5 and 532.8 eV, respectively assigned to lattice oxygen O^{2-} (O_{latt}), adsorbed oxygen (O^-/O_2^{2-}), hydroxyl (-OH/O_2) and physisorbed water.[36] The O_{ads}/O_{latt} ratio (of 2.16) is markedly increased for red-LNO-700 relative to LNO-900 and LNO-700 (both 0.46), as reported in **Table S2**. This increase is consistent with surface structural defects (e.g. steps, kinks and grain boundaries) formed in the RP phase during thermal reduction. La and Ni XP spectra for the LNO samples are shown in **Fig. S4**, wherein La 3*d* and Ni 2*p* peaks are observed with binding energies spanning 840 to 885 eV. Overlap of the La $3d_{3/2}$ and Ni $2p_{3/2}$ spectra, and the presence of satellite peaks, hinders deconvolution of Ni features and assignment of specific oxidation states as previously reported.[37, 38] Although it is challenging to directly identify Ni^{3+} and/or Ni^{2+} states, XPS results in **Fig. S4** reveal similar envelopes for LNO-700 and LNO-900, whereas red-LNO-700 exhibits a distinct peak at 852.6 eV attributable to Ni metal (Ni^0), evidencing significant reduction of Ni^{3+} in red-LNO-700.

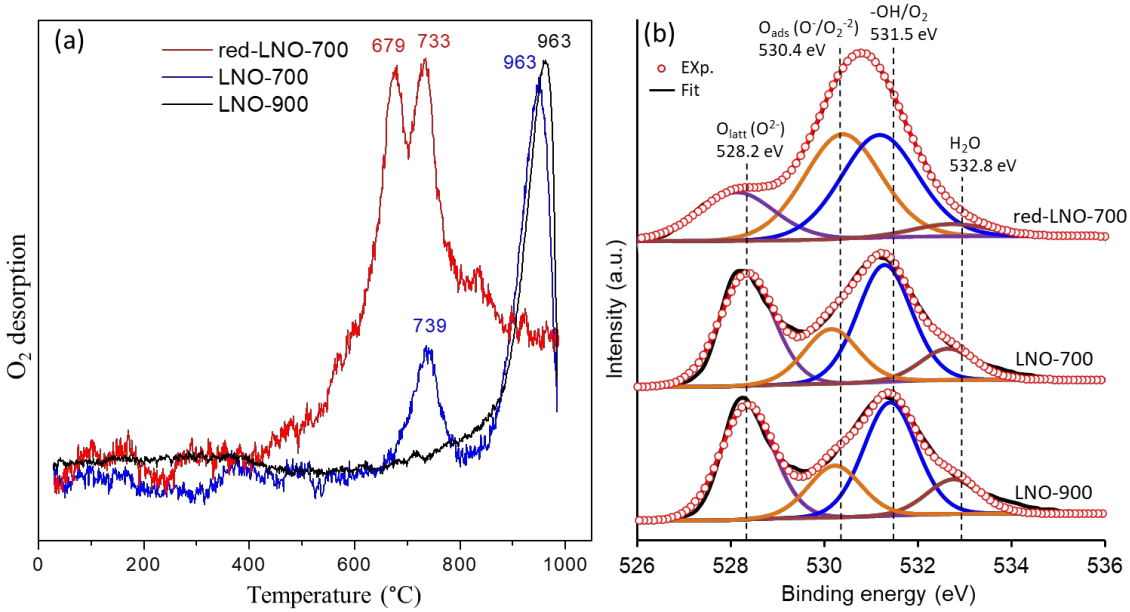

Fig. 3. (a) O_2-TPD profiles, and (b) O 1s XP spectra of LNO materials.

2.1 Electrocatalytic Performance

Linear sweep voltammetry (LSV) curves of LNO materials under alkaline conditions (**Fig. 4a**) revealed the lowest onset potential (at 10 mA.cm^{-2} current density) for red-LNO-700 of 380 mV, superior to that for LNO-700 (410 mV) and LNO-900 (430 mV). This performance is superior to the OER activity previously reported for $LaNiO_3$ synthesised by sol-gol method (600 mV). [39] Note that the carbon fiber paper (CFP) support makes negligible contribution to the measured current density. The OER activity of red-LON-700 also exceeds that of a benchmark IrO_2 catalyst for potentials >1.7 V. Comparison at 500 mV overpotential (**Fig. 4a inset**) highlights the excellent performance of red-LNO-700, which exhibits a current density of 104 mA cm^{-2}, respectively two and five times greater than those of LNO-700 (35 mA cm^{-2}) and LNO-900 (19 mA cm^{-2}), and ~10 % greater than IrO_2. Note that red-LNO-700 significantly outperforms a pure NiO control sample (**Fig. S5**), requiring a lower overpotential of 380 eV, whereas NiO requires an overpotential of 477 eV to reach the same current density. We can therefore neglect possible contributions from NiO phases to the enhanced activity observed for red-LNO-700. Corresponding Tafel plots (**Fig. 4b**) offer insight into the kinetics of OER. The red-LNO-700 electrocatalyst has the lowest Tafel slope of 71 mV.dec^{-1}, significant smaller than those for IrO_2 (76.9 mV dec^{-1}), LNO-700 (90 mV.dec^{-1}) and LNO-900 (104 mV.dec^{-1}), indicating the fastest OER. The good OER activity and fast kinetics of red-LNO-700 are attributed to surface defect formation. Particle size effects on electrocatalytic performance are previously reported.[40] The particle size of synthesised LNO samples increases with synthesis temperature from 700 °C to 900 °C, in accordance with the N_2 porosimetry data (**Fig. 1a** and **Table S1**) which show a converse decrease in surface area. However, as **Table S1** shows, the red-LNO-700 and LNO-700 samples possess similar specific surface areas and perovskite crystallite sizes, yet the reduced (defective) sample exhibits a lower onset potential and five times greater current density (OER activity) at 500 mV overpotential (**Fig. 4a**). Hence in our system, perovskite specific surface area/particle size influence OER performance much less than the stoichiometry.

Fig. 4c shows multistep chronopotentiometric curves for LNO electrodes, wherein the current density was increased stepwise from 8 mA cm^{-2} to 40 mA cm^{-2}, being held for 60 s at each step. The potential of red-LNO-700 quickly stabilised at each step, even for a high current density of 40 mA.cm^{-2}. This contrasted with

LNO-700 and LNO-900 materials, which required increasingly high potentials relative to red-LNO-700 to achieve higher current densities (24-40 mA cm^{-2}), and furthermore required rising potentials to maintain constant current densities. These observations evidence better stability and lower mass transport resistance for red-LNO-700 than its LNO-700 and LNO-900 counterparts. The long-term stability of red-LNO-700 was also investigated at 10 mA.cm^{-2} (**Fig. 4d**); the potential exhibited only a slight increase over 10 h, suggesting rapid dissipation of reactively-formed oxygen bubbles and excellent durability. The enhanced OER performance of red-LNO-700 is attributed to its high concentration of surface defects which facilitate adsorption of water and reactive intermediates such as *OH, *O, and *OOH radicals. The microstructure of the red-LNO-700 samples was examined by TEM following the stability test (**Fig. S6**), and evidenced negligible change in crystallinity, consistent with a stable, defective structure.

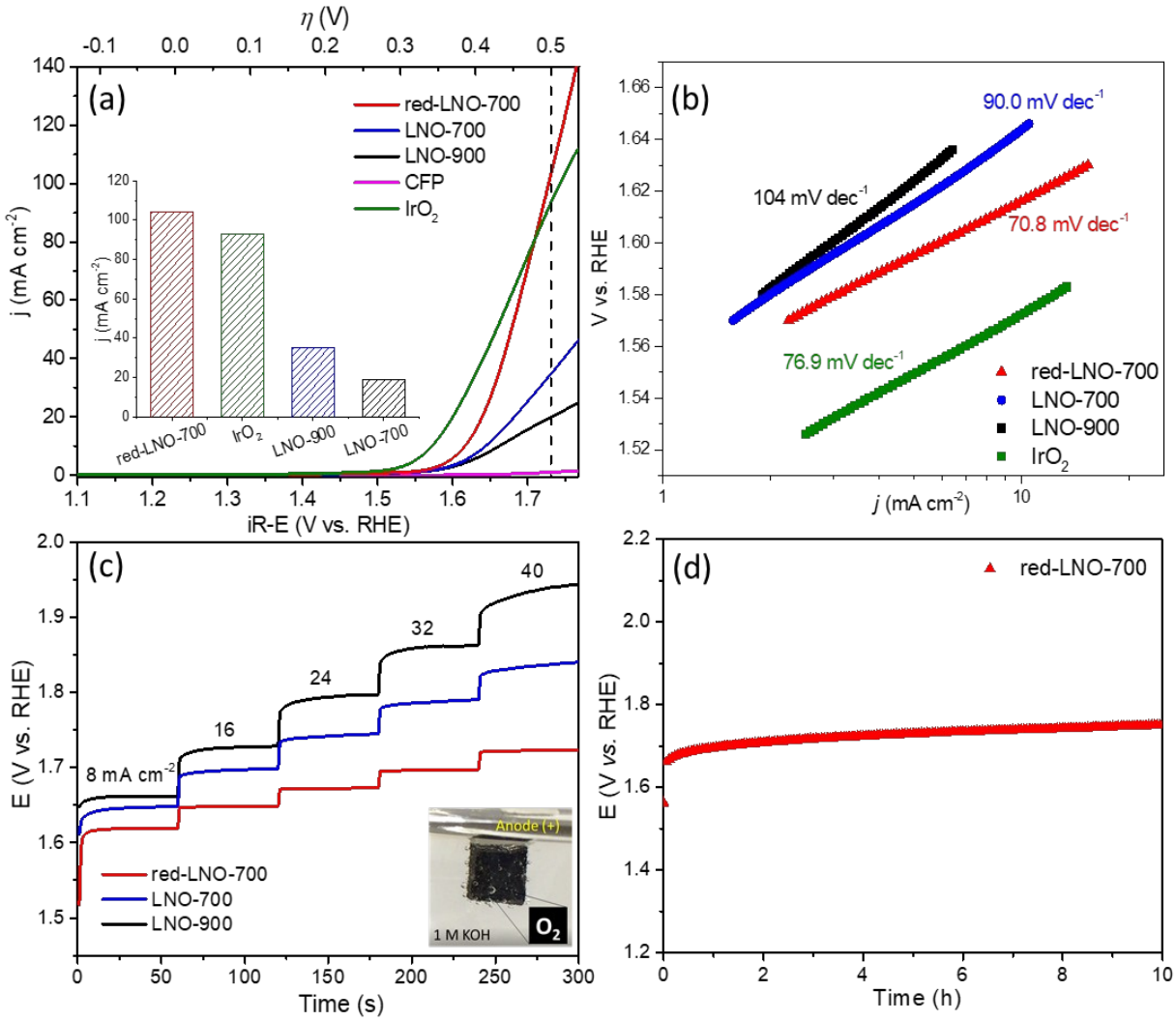

Fig. 4. (a) Linear sweep voltammetry curves toward OER with 85% *iR*-correction, (b) corresponding Tafel plots with 85% *iR*-correction, (c) multi-step chronopotentiometric (CP) curves of LNO at varying current

densities without *iR*-correction, and (d) long-term stability test without *iR*-correction at 10 mA cm^{-2} in 1 M KOH.

Electrochemical impedance spectroscopy (EIS) was subsequently used to study the impendence behavior of LNO electrocatalysts (**Fig. 5a**). Half-circle curves are presented in the resulting Nyquist plots, which can be fitted to the equivalent circuit (**Fig. 5a inset**). The solution resistance (R_s) between the working and reference electrodes was ~4-5 Ω in all cases. The half-circle diameter represents the charge transfer resistance (R_{ct}) at the interface between electrolyte and electrocatalyst, and was significantly smaller for red-LNO-700 (151 Ω) than LNO-700 (246 Ω) or LNO-900 (260 Ω), suggesting faster interfacial charge transfer rate for the former, attributed to surface defects whose presence can tune surface electronic states and increase conductivity.[41] The electrochemically active surface area (ECSA) of LNO materials was evaluated by measuring their double-layer capacitances (C_{dl}) in non-Faradaic potential regions. Cyclic voltammetry was performed at 0.87-0.97 V (versus RHE) at scan rates spanning 100-600 $mV.s^{-1}$ (**Fig. S7**). The C_{dl} was obtained from slopes of linear fits to plots of scan rate against current density (**Fig. 5b**); these reveal an increased C_{dl} (0.95 $mF.cm^{-2}$) for red-LNO-700 compared with LNO-700 (0.80 mF cm^{-2}) and LNO-900 (0.34 mF cm^{-2}), indicating a proportionally greater ECSA for the reduced LNO electrocatalyst, which may also contribute to its improved OER performance.

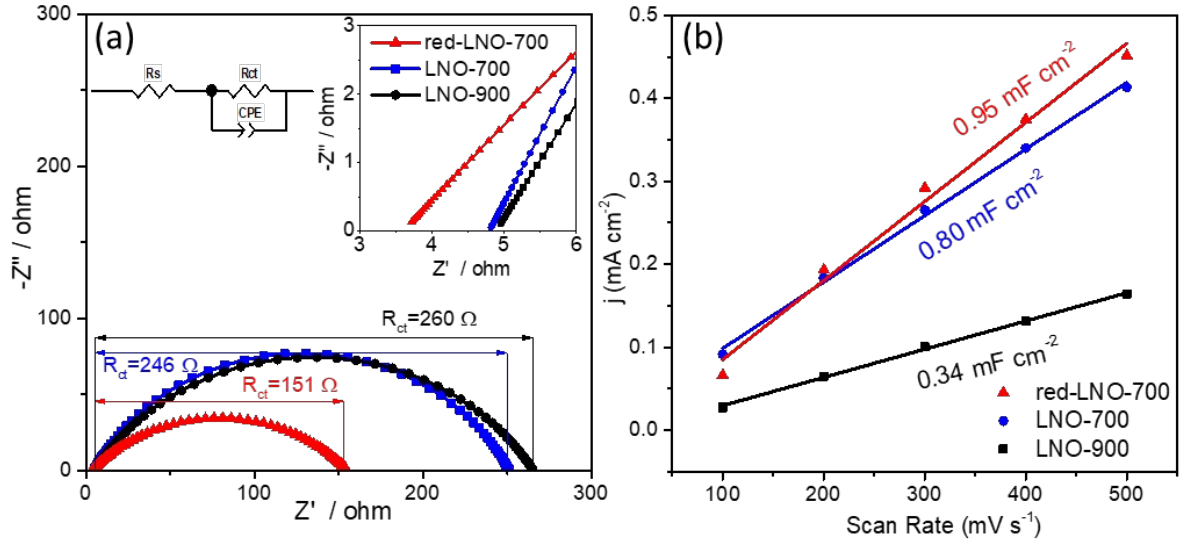

Fig. 5. (a) Nyquist plots of LNO electrocatalysts at 1.6 V vs RHE (inset shows the equivalent circuit), and (b) double layer charging current density as a function of scan rate for C_{dl} determination.

2.2 Density Functional Theory Calculations

Atomistic insight into LNO surfaces was obtained from first-principles calculations based on density functional theory (DFT); details are provided in the Experimental and results are summarised in **Fig. 6** and **Fig. S8**. The surface formation energy, E_{surf}, and oxygen vacancy (V_O) formation energy, E_{vac}, for [100], [110] and [111] planes of LNO were computed. The resulting surface energies were practically independent of crystal orientation (**Fig. S8**), consistent with the wide range of planes observed in **Fig. 2j**; E_{surf} values for [100], [110] and [111] surfaces were 0.105, 0.143 and 0.108 eV.Å^{-2} respectively.

Values of E_{vac} were modest for all three low index surfaces (**Fig. 6a**), and in all cases the formation of surface V_O was energetically favoured with respect to lattice V_O (**Fig. 6a-b**). For the [110] surface apparent in **Fig. 2j**, E_{vac}^{surf} = 1.89 eV versus E_{vac}^{latt} = 2.43 eV, in accordance with the O_2-TPD profile for red-LNO-700 wherein abundant surface V_O were observed. The ease of forming surface V_O reflects the lower coordination number for surface versus bulk O atoms. Additional bulk E_{vac} calculations were also performed employing increasingly large simulation cells to examine whether short or mid-range interactions occur between multiple V_O (**Fig. 6c**). For V_O-V_O distances spanning 7.5-12.5 Å, E_{vac} varied by <4 %, suggesting minimal interactions between nearby oxygen vacancies, which may thus be uniformly distributed throughout the LNO lattice, and minimal energetic penalty to multiple vacancy formation; the latter may explain the high V_O concentration attained for the red-LNO-700 electrocatalyst.

The partial density of electronic states, pDOS, was also calculated for the [110] LNO system, with and without inclusion of a surface V_O (**Fig. 6d**). Highest-energy occupied states appearing just below the Fermi edge correspond to highly hybridised *d*-Ni and *p*-O orbitals, whereas the lowest-energy unoccupied states present at ~2 eV above the Fermi edge correspond to highly hybridised *d*-La and *p*-O orbitals. A significant density of highly hybridised *d*-Ni and *p*-O orbitals also uniformly spanned the energy interval $0 \leq E\text{-}E_F \leq 2$ eV, which are expected to confer good electronic transport properties, and consequently good OER activity, to associated LNO surfaces as observed experimentally observed (**Fig. 4**). Although the electronic band structure of stoichiometric and oxygen-deficient LNO surface are similar, the pDOS close to the Fermi edge

is larger for the latter (**Fig. 6d**), suggesting that V_O formation accompanying thermal reduction should improve electronic transport and hence OER activity as seen for red-LNO-700. Note that previous experimental and theoretical studies suggest *lattice* oxygen vacancies lower the conductivity of LNO.[42, 43] Our first-principles DFT simulations performed for bulk LNO and LNO thin films containing exclusively lattice oxygen vacancies corroborate such findings (**Fig. S9**), and highlight that the increased pDOS at the Fermi level in **Fig. 6d** is only observed for *surface* oxygen vacancies, which are more readily created for LNO thin films. These calculations demonstrate the importance of point defect topology on tuning the transport and catalytic properties of perovskite nickelates.

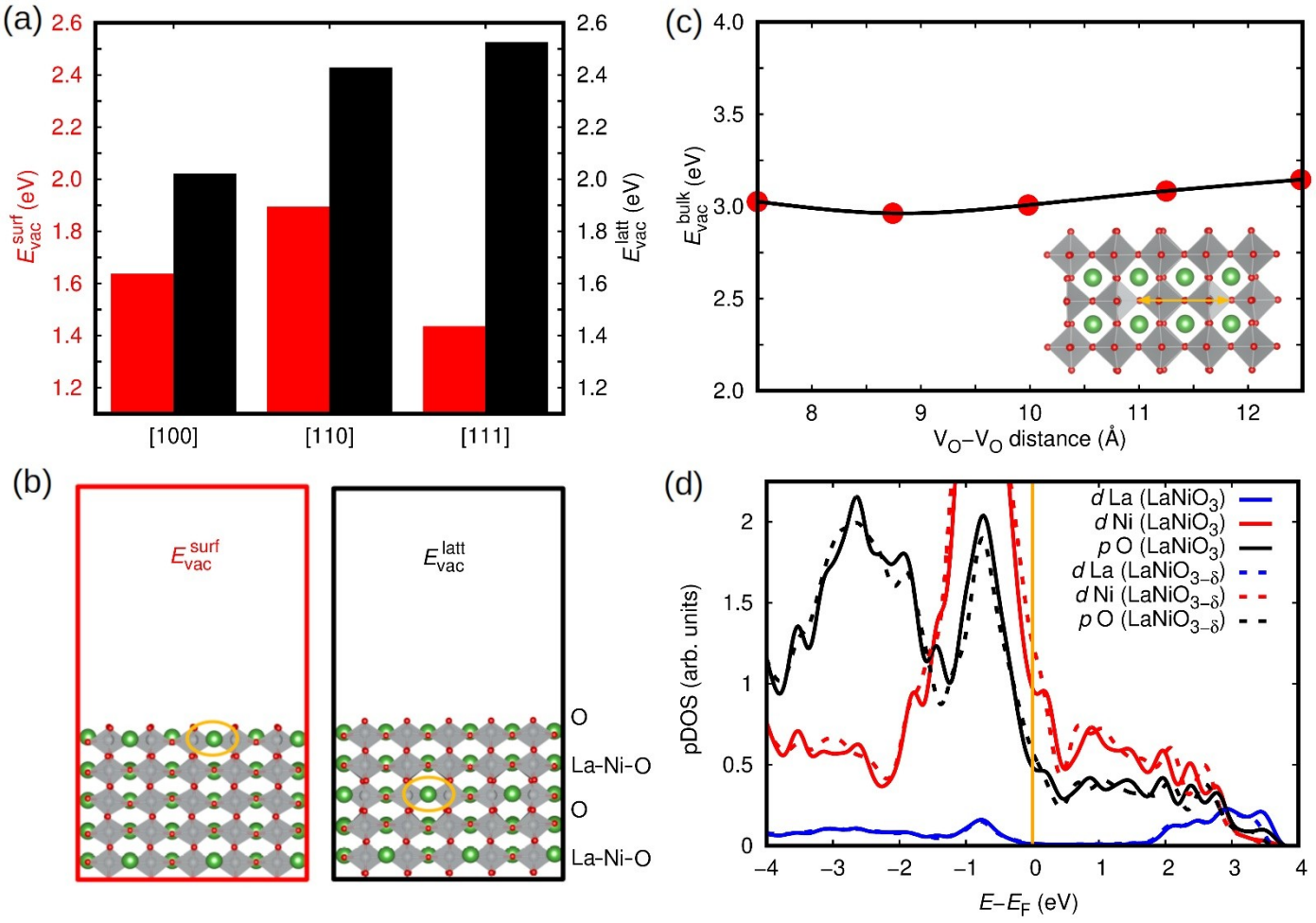

Fig. 6. First-principles DFT results obtained for the oxide perovskite $LaNiO_3$ (LNO). (a) Formation energy of surface and lattice oxygen vacancies calculated for LNO slabs expressed as a function of crystal orientation. (b) Sketch of the slab supercell systems employed for the E_{vac} calculations. (c) Formation energy of oxygen vacancies calculated for bulk LNO and expressed as a function of the distance between point

defects. (d) Density of electronic states (pDOS) for *d*-Ni, *p*-O and *d*-La orbitals calculated for a perfectly stoichiometric and a non-stoichiometric (surface oxygen vacancy) LNO thin film; the Fermi energy level has been shifted to zero in all the cases. La, Ni and O atoms are represented with green, grey and red spheres, respectively.

3. Conclusions

A family of $LaNiO_3$ (LNO) perovskite electrocatalysts were prepared by a simple sol-gel protocol in the presence of CTAB and citric acid structural modifiers and subsequent thermal processing. Calcination at 700 °C yields a macroporous material with modest surface area (~7 $m^2.g^{-1}$); higher temperature calcination collapses the porosity and surface area. HAADF-STEM, XPS and O_2-TPD analyses reveal that a 450 °C hydrogen reduction of the 700 °C calcined LNO induces significant surface defects, notably a high concentration of surface oxygen vacancies. The resulting red-LNO-700 electrocatalyst exhibits a significantly higher current density (10 $mA.cm^{-2}$) at lower overpotential (380 mV), and with faster kinetics (70.8 $mV.dec^{-1}$ Tafel slope) and superior stability, to either unreduced LNO for the oxygen evolution reaction (OER). For overpotentials >500 mV, red-LNO-700 is also more active than a commercial 10 wt% IrO_2 electrocatalyst. Quantum chemical calculations suggest that oxygen vacancy formation is relatively facile over low index LNO surfaces, and modifies the resulting electronic band structure to promote electrical conductivity relative to a stoichiometric surface, consistent with a higher rate of interfacial change transfer experimentally observed. Surface defect formation offers a simple strategy to significantly improve the OER reaction for water splitting, and hence develop low cost technologies for renewable energy production.

4. Experimental Section

4.1. Catalyst Synthesis

A modified sol-gel method [21], incorporating a cetyl ammonium bromide (CTAB) cationic surfactant, was used to prepare high surface area and porous $LaNiO_3$ (LNO) perovskites. 4 mmol ($Ni(NO_3)_2$ (Sigma-Aldrich, 99.9%), 4 mmol $La(NO_3)_3.6H_2O$ (Sigma-Aldrich, 99.9%), 8 mmol citric acid and 4 mmol CTAB (Sigma-

Aldrich, >99%) was dissolved into 80 mL distilled water under magnetic stir at room temperature. The transparent solution was dried at 120 °C for 24 h in oven. Surface defects were subsequently generated through thermal processing. The oven dried samples were first calcined at 700 °C or 900 °C (ramp rate 5°C.min^{-1}) for 4 h to obtain LNO-700 and LNO-900, respectively. The LNO-700 was subsequently heated under flowing 5 vol% H_2/Ar (20 ml.min^{-1}) to 450 °C (ramp rate 5 °C.min^{-1}) for 2 h. The resulting was cooled under Ar (20 ml.min^{-1}) to room temperature and stored in a desiccator and denoted red-LNO-700.

4.2. Electrode Preparation

The working electrode was prepared by drop-casting the catalyst ink made from 500 µL ethanol, 475 µL distilled water, 25 µL Nafion (5 wt % in lower aliphatic alcohols and water, Sigma-Aldrich), 5 mg $LaNiO_3$ or IrO_2 (10 wt% IrO_2 on carbon powder purchased from Advanced Materials Manufacturer) catalyst and 1 mg carbon black onto a carbon fibre paper (CFP) electrode (0.25 cm^2) with a loading mass of 0.28 mg.cm^{-2}.

4.3. Electrocatalytic Tests

Three electrode cell system was used to investigate the OER catalytic performance of the LNO perovskites. Saturated calomel electrode (SCE) and Pt wire are applied as reference and counter electrode, while the as-prepared CFP electrode with perovskite loading is used as a working electrode. All tests were performed in oxygen saturated 1 M KOH (potassium hydroxide, 99.99 % trace metals basis, Sigma-Aldrich) solution at a scan rate of 5 mV/s. The polarisation curve of LNO perovskite relative to the reversible hydrogen electrode (RHE) was recorded. All linear sweep voltammetry (LSV) curves are *iR* corrected (85 %). The stability test was carried out in a three-electrode system using SCE and Pt plate as reference and counter electrode for 10 h in 1 M KOH.

4.4. First-principles Calculations

Density functional theory (DFT) calculations based on the local spin density approximation (LDA) [44, 45] were performed using VASP software. [46] The 3*d* electrons of Ni were treated at the bare LDA level, which has been shown to be the most realistic way to model bulk LNO. [47] Wave functions were represented in a plane-

wave basis set truncated at 750 eV, and a Monkhorst-Pack k-point grid of 12x12x12 was used for reciprocal-space integrations within the first Brillouin zone (IBZ) of a 5-atoms perovskite unit cell. The "*projected augmented wave*" method was used to represent the ionic cores considering the following electronic states as valence: La 5*d*6*s*5*p*, Ni 4*s*3*d* and O 2*s*2*p*. Geometry relaxations were performed to optimise the lattice vectors of cubic LNO (space group *Pm-3m*) by using a conjugate-gradient algorithm that optimised the volume and shape of the unit cell as well as the atomic positions. The geometry relaxations were halted once the forces in all the atoms were smaller than 0.01 eV/Å.

LNO slabs with orientations [100], [110] and [111] were modelled with stacks of 6-7 LNO layers described by the chemical formula $La_{28}Ni_{28}O_{84}$. A vacuum region of 25 Å was considered in all the simulations, and periodic boundary conditions were applied along with the three Cartesian directions. The surface formation energy of stoichiometric [100], [110] and [111] LNO was calculated as:

$$E_{surf} = (E_{slab} - E_{bulk})/2A$$

where E_{slab} is the energy of the stoichiometric LNO slab, E_{bulk} the energy of bulk LNO (considering the same number of formula units as in the slab system), and A the area of the interface formed by the LNO slab and vacuum. Likewise, the formation energy of oxygen vacancies for the [100], [110] and [111] LNO slabs was estimated with the formula:

$$E_{vac} = E_{slab}(La_{28}Ni_{28}O_{83}) + \mu_O - E_{slab}(La_{28}Ni_{28}O_{84})$$

where the first term in the right-hand side of the equation corresponds to the energy of a non-stoichiometric slab created by removing one oxygen atom from $La_{28}Ni_{28}O_{84}$, and μ_O represents the chemical potential of an oxygen atom taken equal to -5.0 eV. [48] Oxygen vacancies located both in the surface and interior of the slabs were considered in our DFT simulations.

Supporting Information

Supporting Information is available from the Wiley Online Library or from the author.

Acknowledgements

Hamidreza Arandiyan acknowledges financial support through the University of Sydney Research Fellowship (G197582) program and ARC DP200100313. The authors acknowledge the facilities at Sydney Microscopy & Microanalysis and Sydney Nano at the University of Sydney and the facilities, and the scientific and technical assistance of the RMIT Microscopy & Microanalysis Facility (RMMF), a linked laboratory of the Australian Microscopy & Microanalysis Research Facility.

Conflicts of interest

There are no conflicts to declare.

References

[1. M. Armand and J. M. Tarascon, *Nature*, 2008, **451**, 652-657.
2. K. M. Abraham, *Journal of The Electrochemical Society*, 1996, **143**, 1.
3. J. Rossmeisl, A. Logadottir and J. K. Nørskov, *Chemical Physics*, 2005, **319**, 178-184.
4. Y. Wang, D. Y. C. Leung, J. Xuan and H. Wang, *Renewable and Sustainable Energy Reviews*, 2016, **65**, 961-977.
5. D. Friebel, M. W. Louie, M. Bajdich, K. E. Sanwald, Y. Cai, A. M. Wise, M.-J. Cheng, D. Sokaras, T.-C. Weng, R. Alonso-Mori, R. C. Davis, J. R. Bargar, J. K. Nørskov, A. Nilsson and A. T. Bell, *J. Am. Chem. Soc.*, 2015, **137**, 1305-1313.
6. D. K. Bediako, B. Lassalle-Kaiser, Y. Surendranath, J. Yano, V. K. Yachandra and D. G. Nocera, *Journal of the American Chemical Society*, 2012, **134**, 6801-6809.
7. T. Zhao, Y. Wang, S. Karuturi, K. Catchpole, Q. Zhang and C. Zhao, *Carbon Energy*, 2020, **2**, 582-613.
8. M. H. Seo, H. W. Park, D. U. Lee, M. G. Park and Z. Chen, *ACS Catal.*, 2015, **5**, 4337-4344.
9. Y. Matsumoto, *Journal of The Electrochemical Society*, 1980, **127**, 811.
10. R. A. Rincón, E. Ventosa, F. Tietz, J. Masa, S. Seisel, V. Kuznetsov and W. Schuhmann, *ChemPhysChem*, 2014, **15**, 2810-2816.
11. J. Suntivich, K. J. May, H. A. Gasteiger, J. B. Goodenough and Y. Shao-Horn, *Science*, 2011, **334**, 1383-1385.
12. G. Karlsson, *Journal of Power Sources*, 1983, **10**, 319-331.
13. Y. Lee, J. Suntivich, K. J. May, E. E. Perry and Y. Shao-Horn, *The Journal of Physical Chemistry Letters*, 2012, **3**, 399-404.
14. W. G. Hardin, D. A. Slanac, X. Wang, S. Dai, K. P. Johnston and K. J. Stevenson, *The Journal of Physical Chemistry Letters*, 2013, **4**, 1254-1259.

15. J. Chakhalian, J. M. Rondinelli, J. Liu, B. A. Gray, M. Kareev, E. J. Moon, N. Prasai, J. L. Cohn, M. Varela, I. C. Tung, M. J. Bedzyk, S. G. Altendorf, F. Strigari, B. Dabrowski, L. H. Tjeng, P. J. Ryan and J. W. Freeland, *Physical Review Letters*, 2011, **107**, 116805.
16. C. Zhao, N. Li, R. Zhang, Z. Zhu, J. Lin, K. Zhang and C. Zhao, *ACS Appl. Mater. Interfaces*, 2019, **11**, 47858-47867.
17. Y. Lu, A. Ma, Y. Yu, R. Tan, C. Liu, P. Zhang, D. Liu and J. Gui, *ACS Sustain. Chem. Eng.*, 2019, **7**, 2906-2910.
18. J. T. Mefford, X. Rong, A. M. Abakumov, W. G. Hardin, S. Dai, A. M. Kolpak, K. P. Johnston and K. J. Stevenson, *Nat. Commun.*, 2016, **7**, 11053.
19. J. R. Petrie, V. R. Cooper, J. W. Freeland, T. L. Meyer, Z. Zhang, D. A. Lutterman and H. N. Lee, *J. Am. Chem. Soc.*, 2016, **138**, 2488-2491.
20. P. L. Gai-Boyes, *Catalysis Reviews*, 1992, **34**, 1-54.
21. Y. Wang, H. Arandiyan, X. Chen, T. Zhao, X. Bo, Z. Su and C. Zhao, *The Journal of Physical Chemistry C*, 2020, DOI: 10.1021/acs.jpcc.0c01135.
22. Y. Wang, X. Shen, H. Arandiyan, Y. Yin, F. Sun, X. Chen, M. Garbrecht, L. Han, G. G. Andersson and C. Zhao, *Journal of Power Sources*, 2020, **478**, 228748.
23. T. Zhao, Y. Wang, X. Chen, Y. Li, Z. Su and C. Zhao, *ACS Sustainable Chemistry & Engineering*, 2020, **8**, 4863-4870.
24. Y. Sun, R. Li, X. Chen, J. Wu, Y. Xie, X. Wang, K. Ma, L. Wang, Z. Zhang, Q. Liao, Z. Kang and Y. Zhang, *Advanced Energy Materials*, 2021, **11**, 2003755.
25. M.-J. Choi, T. L. Kim, J. K. Kim, T. H. Lee, S. A. Lee, C. Kim, K. Hong, C. W. Bark, K.-T. Ko and H. W. Jang, *Nano Letters*, 2020, **20**, 8040-8045.
26. Y. Liu, Z. Wang, J.-P. M. Veder, Z. Xu, Y. Zhong, W. Zhou, M. O. Tade, S. Wang and Z. Shao, *Advanced Energy Materials*, 2018, **8**, 1702604.
27. H. Wang, J. Qi, N. Yang, W. Cui, J. Wang, Q. Li, Q. Zhang, X. Yu, L. Gu, J. Li, R. Yu, K. Huang, S. Song, S. Feng and D. Wang, *Angewandte Chemie International Edition*, 2020, **59**, 19691-19695.
28. N.-I. Kim, Y. J. Sa, T. S. Yoo, S. R. Choi, R. A. Afzal, T. Choi, Y.-S. Seo, K.-S. Lee, J. Y. Hwang, W. S. Choi, S. H. Joo and J.-Y. Park, *Science Advances*, 2018, **4**, eaap9360.
29. H. Lee, O. Gwon, K. Choi, L. Zhang, J. Zhou, J. Park, J.-W. Yoo, J.-Q. Wang, J. H. Lee and G. Kim, *ACS Catalysis*, 2020, **10**, 4664-4670.
30. M. Khazaei, A. Malekzadeh, F. Amini, Y. Mortazavi and A. Khodadadi, *Crystal Research and Technology*, 2010, **45**, 1064-1068.
31. G. Q. Liu, Z. G. Jin, X. X. Liu, T. Wang and Z. F. Liu, *Journal of Sol-Gel Science and Technology*, 2007, **41**, 49-55.
32. Z. A. ALOthman, *Materials*, 2012, **5**, 2874-2902.
33. E. Detemple, Q. M. Ramasse, W. Sigle, G. Cristiani, H.-U. Habermeier, B. Keimer and P. A. v. Aken, *Journal of Applied Physics*, 2012, **112**, 013509.
34. S. Ponce, M. A. Peña and J. L. G. Fierro, *Applied Catalysis B: Environmental*, 2000, **24**, 193-205.
35. H. Zhu, P. Zhang and S. Dai, *ACS Catalysis*, 2015, **5**, 6370-6385.
36. P. Li, C. Tian, W. Yang, W. Zhao and Z. Lü, *Frontiers of Materials Science*, 2019, **13**, 277-287.
37. X. Ning, Z. Wang and Z. Zhang, *Scientific Reports*, 2015, **5**, 8460.
38. S. Mickevicius, S. Grebinskij, V. Bondarenka, B. Vengalis, K. Šliužienė, B. A. Orlowski, V. Osinniy and W. Drube, *Journal of Alloys and Compounds*, 2006, **423**, 107-111.
39. Q. Guo, X. Li, H. Wei, Y. Liu, L. Li, X. Yang, X. Zhang, H. Liu and Z. Lu, *Frontiers in Chemistry*, 2019, **7**.
40. A. J. Esswein, M. J. McMurdo, P. N. Ross, A. T. Bell and T. D. Tilley, *The Journal of Physical Chemistry C*, 2009, **113**, 15068-15072.
41. Y. Cheng, H. Song, H. Wu, P. Zhang, Z. Tang and S. Lu, *Chemistry – An Asian Journal*, 2020, **15**, 3123-3134.
42. R. D. Sánchez, M. T. Causa, A. Caneiro, A. Butera, M. Vallet-Regí, M. J. Sayagués, J. González-Calbet, F. García-Sanz and J. Rivas, *Physical Review B*, 1996, **54**, 16574-16578.
43. A. Malashevich and S. Ismail-Beigi, *Physical Review B*, 2015, **92**, 144102.
44. W. Kohn and L. J. Sham, *Physical Review*, 1965, **140**, A1133-A1138.

45. P. Hohenberg and W. Kohn, *Physical Review*, 1964, **136**, B864-B871.
46. G. Kresse and J. Furthmüller, *Physical Review B*, 1996, **54**, 11169-11186.
47. M. Gibert, P. Zubko, R. Scherwitzl, J. Íñiguez and J.-M. Triscone, *Nature Materials*, 2012, **11**, 195-198.
48. C. Cazorla, *Physical Review Applied*, 2017, **7**, 044025.

Table of Contents

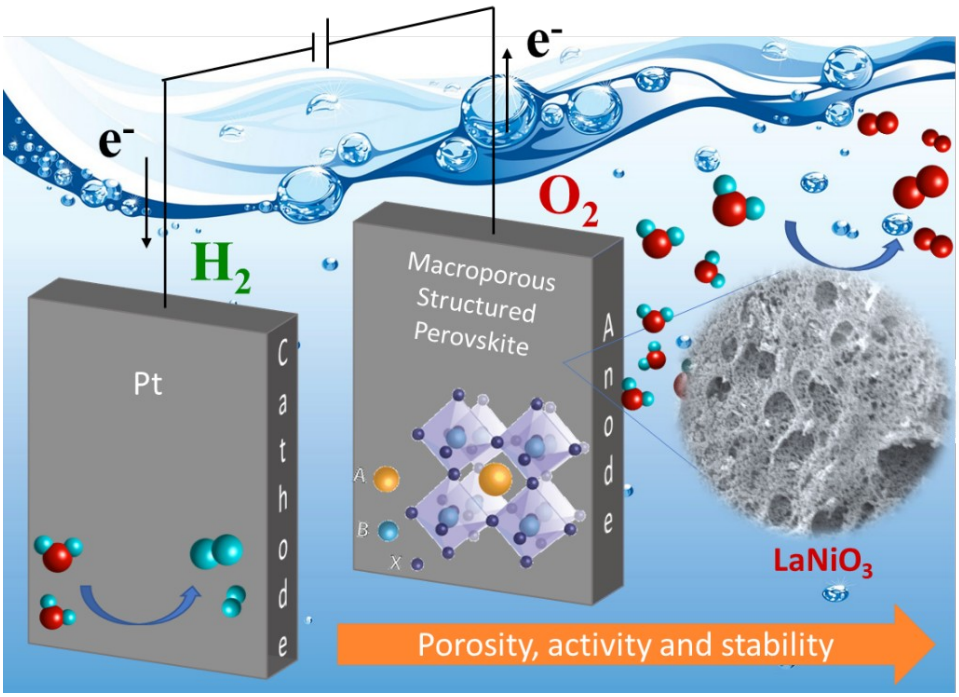

Surface defect formation modifies the electronic properties of macroporous $LaNiO_3$ perovskites, promoting the oxygen evolution reaction.